Biophysical Journal, Volume 98

**Supporting Material**

# Protein collective motions coupled to ligand migration in Myoglobin

Yasutaka Nishihara, Shigeki Kato, and Shigehiko Hayashi

# Supporting Material for : Protein Collective Motions Coupled to Ligand Migration in Myoglobin

Yasutaka Nishihara, Shigeki Kato, and Shigehiko Hayashi[1]

Department of Chemistry, Graduate School of Science,
Kyoto University, Kitashirakawa, Sakyo-ku, Kyoto 606-8502, Japan

[1]To whom correspondence should be addressed; E-mail: hayashig@kuchem.kyoto-u.ac.jp

This material includes supplemental descriptions and figures on.

1. force field parameters and MD simulation protocols,
2. kinetic model used to calculate CO transition rate by MD simulations,
3. three- and one-dimensional free energy maps of the CO migration pathway,
4. a variance-covariance matrix used for the linear response theory (LRT) analysis,
5. external forces used for the LRT analysis,
6. protein responses to the external forces coupled with the Xe4-to-Xe2 and Xe2-to-Xe1 transitions of CO,
7. contributions of principal component (PC) vectors to protein responses coupled with the Xe4-to-Xe2 and Xe2-to-Xe1 transitions of CO,
8. derivation of a generalized Langevin equation given by Eq. (12),
9. expressions of Mean First Passage Time (MFPT), and
10. evaluation of parameters of MFPT and a transition state theory (TST) rate expression.

## 1 Force field parameters and MD simulation protocols

MD simulations were performed by AMBER program package with the parm99 force field (1), TIP3P water model (2) and a set of heme parameters by Giammona and Case (3). The effective partial atomic charges of the unbound CO were set to be

-0.021e and 0.021e on the C and O atoms, respectively, so as to reproduce a dipole moment determined experimentally, $\mu$ = 0.11 Debye. Two parameters of the non-bonded interaction (12-6 Lennard-Jones potential function), a radius and well depth parameter, were set to be 1.85 Å and 0.12 kcal/mol on the C atom, respectively. For the O atom, these were set to be 1.60 Å and 0.20 kcal/mol, respectively. We employed those parameter sets for all MD simulations in the present study as well as metadynamics MD simulations in a previous study by us (4) for calculation of three-dimensional free energy profile of CO migration.

The present two-site point charge model for CO lacks higher order multipole electrostatic interactions. The higher order multipole interactions have been shown to be significant for the description of the vibrational spectra (5–8), which are known to be very sensitive to the electrostatic interaction. However, the free energy profile and the CO migration dynamics are expected to be at least qualitatively described by the two-site model. It is noteworthy that the free energy profile for the CO migration between the distal pocket (DP) and Xe4 obtained by the previous study (4) is in line with that by a recent study by Banushkina and Meuwly (9) where newly developed sets of the force field for heme and CO were employed. For example, the barrier heights of the DP-to-Xe4 transition were computed to be 1.3 kcal/mol in both studies, although the CO-heme electrostatic interaction exists in the initial state where CO occupies DP. Detailed examination of the free energy profile including free energies of the CO binding sites, transition states and one-dimensional projections of the three-dimensional free energy map has been reported in Ref. (4). Furthermore, the ligand migration dynamics and the protein conformational changes for L29W mutant were successfully simulated in a study by Hummer et al. (10), where a two-site charge model was used. Although the lack of the higher order interactions introduces some small errors, in order to keep internal consistency of the linear response analysis, we used the two-site model in the present MD simulations as well as the previous study (4).

Temperature and pressure in the MD simulations were controlled to be 300 K and 1 atm, respectively, by Berendsen algorithm (11). Particle-mesh Ewald algorithm (12) was used for long-range electrostatic interactions, and other short-ranged nonbonding interactions were calculated using a cut-off of 12 Å. A time step was set to be 1.0 fs. The SHAKE algorithm (13) was applied to the bonds including hydrogen atoms.

# 2 Kinetic model used to calculate CO transition rate by MD simulations

The kinetics of a CO migration between DP and Xe4 derived by MFPT theory was compared with the direct 10-ns MD simulations (the simulation (d-i) in Methods). In the 30 trajectories, transitions from DP and to a protein surface or other sites

were observed in 12 trajectories. Thus, $P_{\mathrm{DP}}(t)$ was evaluated with the remaining 18 trajectories. The numbers of the transition between DP and Xe4 observed in the simulations were 26 for forward (DP → Xe4) and 19 for backward (Xe4 → DP). We computed the rate constants for the forward and backward transitions between DP and Xe4 sites, $k_f$ and $k_b$, respectively, by fitting a time evolution of the normalized population $P_{\mathrm{DP}}(t)$ of the two-states model to that obtained by the MD trajectories.

$$P_{\mathrm{DP}}(t) = 1 + \frac{k_f}{k_f + k_b}\left\{e^{-(k_f+k_b)t} - 1\right\} \tag{1}$$

The use of the simple two-states model for the transition between DP and Xe4 is justified as follows. As observed in experiments (14, 15) and in the present study, transitions from the DP and Xe4 to other Xe cavities and the binding to heme are much slower than transition between DP and Xe4. Thus, the DP-Xe4 transition is kinetically well separated from other processes and is expected to be well approximated with the two-states model.

# 3 Three- and one-dimensional free energy maps of the CO migration pathway

The three-dimensional free energy map shown in Fig. 2 was computed by metadynamics simulations carried out previously (4). In the metadynamics simulations, repulsive biasing potential functions acting on the center of mass of CO were adaptively placed in three-dimensional space to enhance sampling of the CO distribution. The simulation found a CO migration pathway from DP to Xe1 via Xe4 and Xe2 as shown in Fig. 2. A three-dimensional free energy map shown in Fig. 2 was also calculated by the metadynamics simulation with a further refinement. Figure S1 shows the one-dimensional free energy profiles of the cavity-to-cavity transition, DP-to-Xe4, Xe4-to-Xe2, and Xe2-to-Xe1, projected onto the line between the centers of those sites (4). Table S1 summarizes the free energies at DP and Xe sites in the migration pathway along with the activation free energies separating those sites.

Table S1: Free energies at the minima of DP, Xe sites and activation free energies of transitions between the neighboring sites (kcal/mol) reported in ref. (4)

| site | DP | → | Xe4 | → | Xe2 | → | Xe1 |
|---|---|---|---|---|---|---|---|
| $\Delta G$ | 0.00 | | -0.40 | | 0.54 | | -0.60 |
| $\Delta G^{\ddagger}$ | | 1.34 | | 2.65 | | 1.42 | |

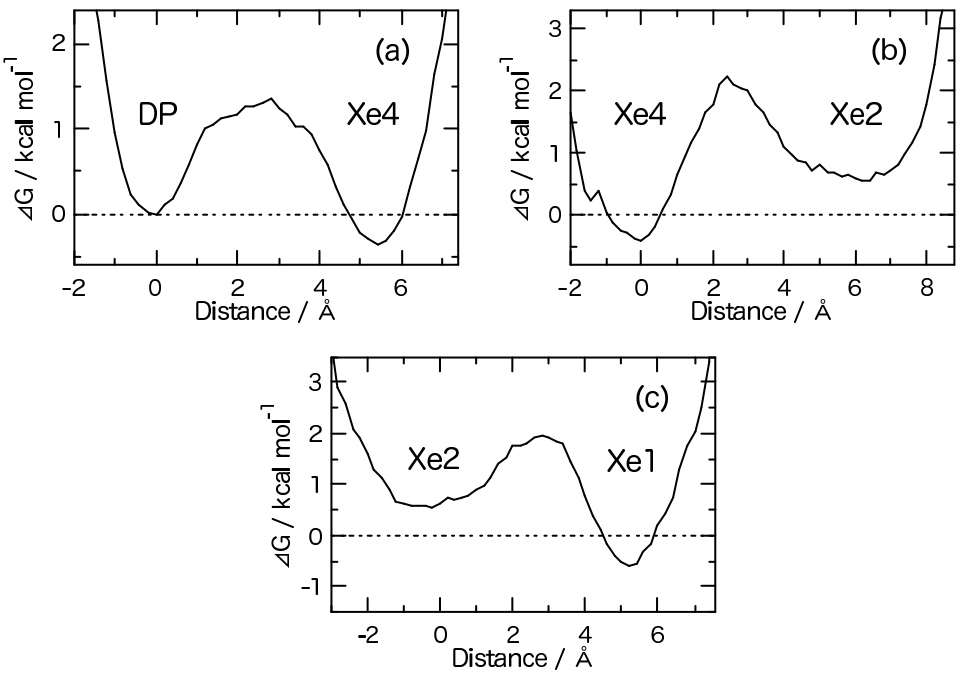


Figure S1: One-dimensional free energy profiles of the cavity-to-cavity transitions of CO, (a) DP-to-Xe4, (b) Xe4-to-Xe2, and (c) Xe2-to-Xe1, computed by a meta-dynamics simulation (4)

# 4 A variance-covariance matrix used for the LRT analysis

A variance-covariance matrix used for the LRT analysis was constructed for coordinates of heavy atoms sampled at every 50 fs from a trajectory computed by the simulation (c) described in Methods. We excluded the coordinates of side chains of residues on the protein surface exposed to bulk solvent from the variance-covariance matrix (see below for a list of the excluded residues), because the fluctuations of those surface groups are very large and thus introduce errors due to deviations from the second order fluctuation. Note that the migration pathway connecting DP, Xe4, Xe2, and Xe1 investigated in the present study goes through the interior of the protein, and is not exposed on the surface of the protein. Hence, no direct interactions of CO with the surface groups are established in the migration along the pathway, and the migration dynamics is little affected by the surface groups. This is consistent with the results by Cohen et al. (16), suggesting that surface groups add no effect on the free energy associated with the ligand migration inside Mb, whereas the free energy inside the protein is influenced by interior residues. Below is a list of the residues whose side chains were truncated.

GLY1, LEU2, SER3, ASP4, GLY5, GLU6, GLN8, GLN9, LEU11, ASN12, GLY15, LYS16, GLU18, ALA19, ASP20, ILE21, ALA22, GLY23, GLU27, ARG31, HR34, GLY35, HIS36, PRO37, GLU38, GLU41, LYS42, ASP44, LYS45, LYS47, HIS48, LEU49, LYS50, THR51, GLU52, ALA53, GLU54, LYS56, ALA57, SER58, GLU59, ASP60, LYS62, LYS63, HIS64, THR66, VAL67, THR70, ALA71, GLY73, GLY74, LYS77, LYS78, LYS79, GLY80, HIS81, GLU83, ALA84, GLU85, LYS87, PRO88, LEU89, GLN91, SER92, THR95, LYS96, HIS97, LYS98, PRO100, ILE101, LYS102, TYR103, GLU105, PHE106, ASP109, ILE112, HIS113, HIS116, SER117, LYS118, HIS119, PRO120, GLY121, ASP122, GLY124, ALA125, ASP126, ALA127, GLN128, GLY129, THR132, LYS133, GLU136, LEU137, ARG139, ASN140, ASP141, ALA143, ALA144, LYS145, LYS147, GLU148, LEU149, GLY150, PHE151, GLN152.

# 5 External forces used for the LRT analysis

First, the molecular origins of the external forces were examined. The external forces coupled with the DP-to-Xe4 transition were calculated, in terms of the van der Waals (vdW) interaction, the electrostatic interaction with a dipole moment of CO, $\mu$ = 0.11 Debye, i.e., the same value as that of the two-site model used in the present MD simulation, and that with a quadrupole moment, respectively. A three-site

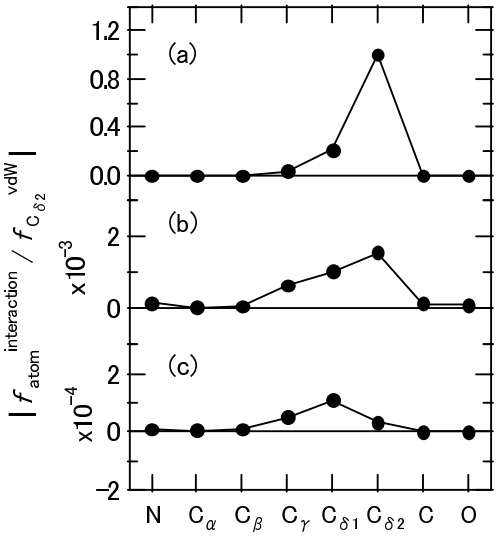


Figure S2: External forces acting on the atoms of Leu29, originated from the non-binding interactions of the CO molecule. (a) van der Waals (vdW), (b) electrostatic with a dipole moment of CO and (c) electrostatic with a quadrupole moment of CO. The forces are scaled by the vdW force acting on $C_{\delta 2}$ atom of Leu29.

model (5) was used to represent the quadrupole moment. CO was put on the position corresponding to the top of the free energy barrier between DP and Xe4 obtained by a previous study (4). For the protein structure of Mb, the average structure of Mb obtained by a 10-ns MD calculation (the simulation (c)) was used. The external forces acting on the heavy atoms of Leu29, to which the largest external forces are applied by the interaction with CO (see text), are shown in Fig. S2. The result shows that the vdW interaction of CO at the transition state for the CO migration process is dominant, and the electrostatic interactions give negligible contributions.

Figure S3 also depicts large external forces acting on the atoms of the protein groups coupled with the cavity-to-cavity transitions, DP-to-Xe4, Xe4-to-Xe2, and Xe2-to-Xe1 calculated by Eq. (6).

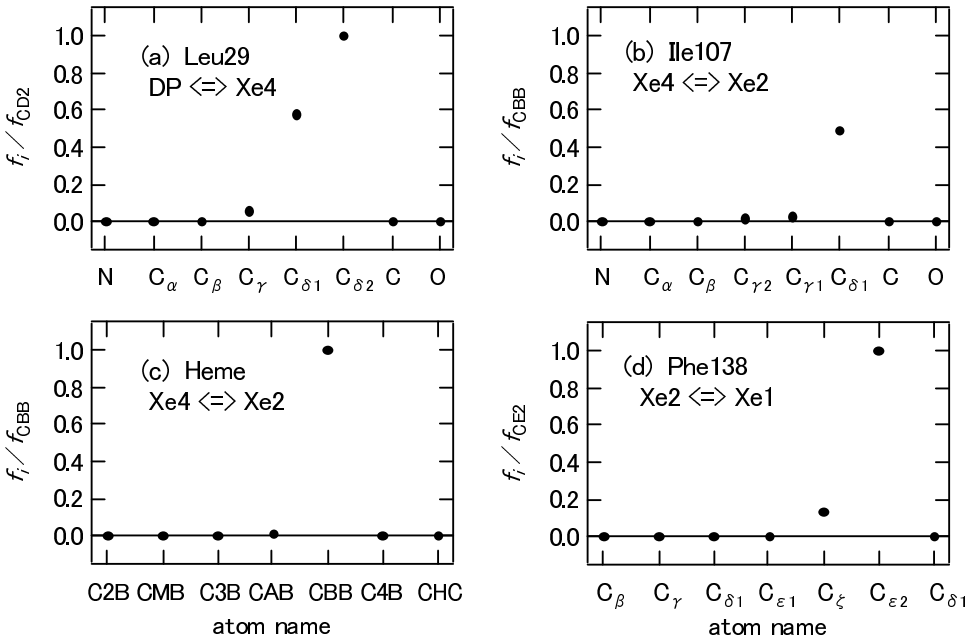


Figure S3: External forces acting on protein groups due to interaction with CO in the transition state regions of the cavity-to-cavity transitions. The forces acting on atoms of (a) Leu29 in the transition between DP and Xe4, (b) Ile107 between Xe4 and Xe2, (c) heme between Xe4 and Xe2, and (d) Phe138 between Xe2 and Xe1 are depicted. The forces are scaled by the maximal force in each transition.

The magnitudes of the external forces were adjusted so as to give the protein responses optimal for the channel openings which minimize potential energies of the system, $V$, at the free energy barrier tops. The potential energy of the system is expressed as

$$V(|\delta \boldsymbol{r}|) = V_{\mathrm{vdW}}(|\delta \boldsymbol{r}|) + \frac{k_{\mathrm{B}}T}{2}\delta \boldsymbol{r}^t \boldsymbol{K} \delta \boldsymbol{r} \qquad \text{(S2)}$$

where $k_{\mathrm{B}}$ is Boltzmann constant, $T$ is a temperature (300 K), $\delta \boldsymbol{r}$ indicates the protein

response and $V_{\mathrm{vdW}}$ is the vdW interaction of CO with the protein groups at the free energy barrier top. $\boldsymbol{K}$ is the inverse of the variance-covariance matrix,

$$\{\boldsymbol{K}\}^{-1}{}_{ij} = \left\langle \Delta r_i \Delta r_j \right\rangle . \tag{S3}$$

As the channel opens, the vdW repulsion decreases because the overlaps of the CO distribution with the protein groups decrease. As contrary, the second term of Eq. (S2), which represents the protein deformation energy in the linear response approximation, increases. Hence the potential energy of the system exhibits a minimum at which the magnitude of the protein response is optimal for the cavity-to-cavity translocation of CO through the channel. The potential energy was therefore used as a measure to determine the optimal magnitude of the protein deformation, i.e., the channel opening along the protein response coordinate.

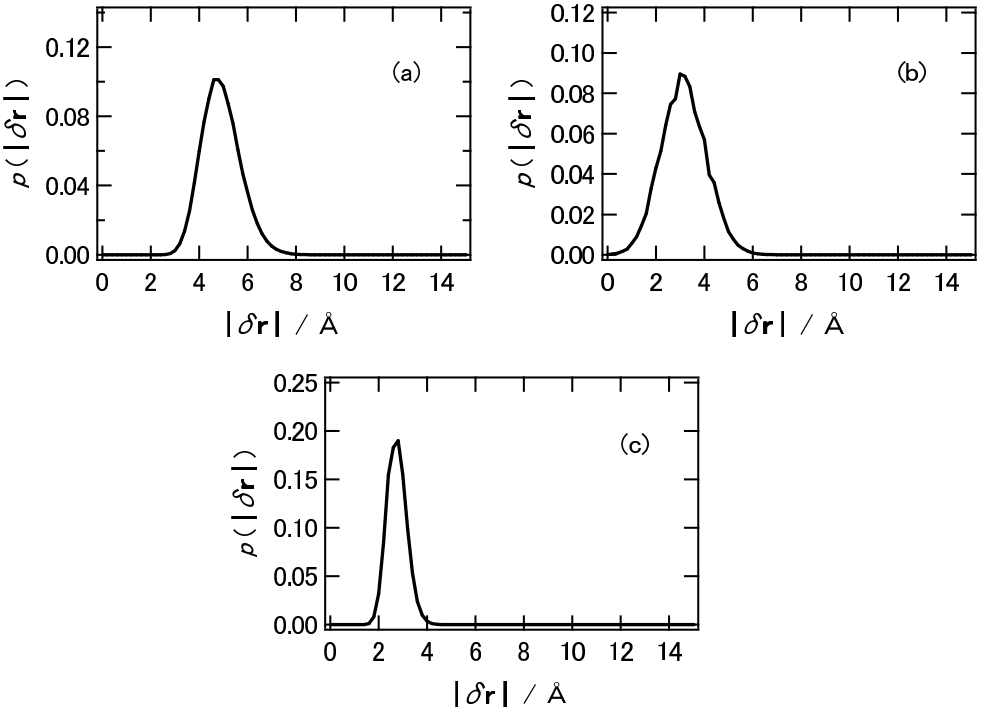


Figure S4: Probability distribution of protein response to the CO migration. The probability distribution of (a) the migration between DP and Xe4, (b) Xe4 and Xe2, and (c) Xe2 and Xe1 are depicted.

Figure S4 depicts probability distributions of V,

$$p(|\delta \boldsymbol{r}|) \propto \exp[-V(|\delta \boldsymbol{r}|)/k_{\mathrm{B}}T]. \tag{S4}$$

As seen Fig. S4, the probability distributions exhibit maxima, i.e., the potential energies of the system exhibit minima, at $|\delta \boldsymbol{r}| = 4.8$ Å in the migration between DP

and Xe4, at $|\delta \boldsymbol{r}|$ = 3.0 Å between Xe4 and Xe2, and at $|\delta \boldsymbol{r}|$ = 2.8 Å between Xe2 and Xe1. The protein responses for the maximum values of $p(|\delta \boldsymbol{r}|)$ are shown in Figs. 3 and S5.

Finally, the external forces for transitions at the barrier tops were examined. The external forces for the transition between DP and Xe4 mainly act on $C_{\delta 2}$ and $C_{\delta 1}$ atoms of Leu29 in the B helix as discussed in the text. Similarly, the external forces for the other transitions were observed to act on relatively localized atoms. For the transition between Xe4 and Xe2, the external forces act on an atom of heme (a terminal carbon atom of a vinyl group at $C_3$) as well as that of a protein side chain ($C_{\delta 1}$ of Ile107). The transition between Xe2 and Xe1 mainly gives forces acting on atoms of Phe138, especially $C_{\epsilon 2}$.

# 6 Protein responses to the external forces coupled with the Xe4-to-Xe2 and Xe2-to-Xe1 transitions of CO

Figure S5 shows protein conformational changes in response to the external forces coupled with the Xe4-to-Xe2 and Xe2-to-Xe1 transitions of CO calculated by Eq. (5). The protein responses to the DP-to-Xe4 transition are depicted in Figs. 3 and 4. Large components of the protein response to the migration between Xe4 and Xe2 are also shown in Figs. 2(b) and S5(a). A vinyl group of heme undergoes a large displacement by the external force acting on the same group, indicating that the vinyl group of heme acts as a gate for the transition. An outward movement of Leu86 at the F helix was also observed. Figures S5(a) and S6(a) also show that collective motions are also induced by the external perturbation in CO migration between Xe4 and Xe2. Compared with the transition between DP and Xe4, the collective motions are small and all helices move almost evenly and slightly. Since the gating motion appears at the cofactor heme, the motion is considered to correlate only weakly with the protein modes. The protein conformational changes for the migration between Xe2 and Xe1 are shown in Figs. 2(b), S5(b) and S6(b). A large outward movement of Phe138 is induced by the external forces acting on the same residue. Collective motions associated with the movement of Phe138 are observed mainly in the regions close to the residue, although the motions are not very extensive compared with those for the transition between DP and Xe4.

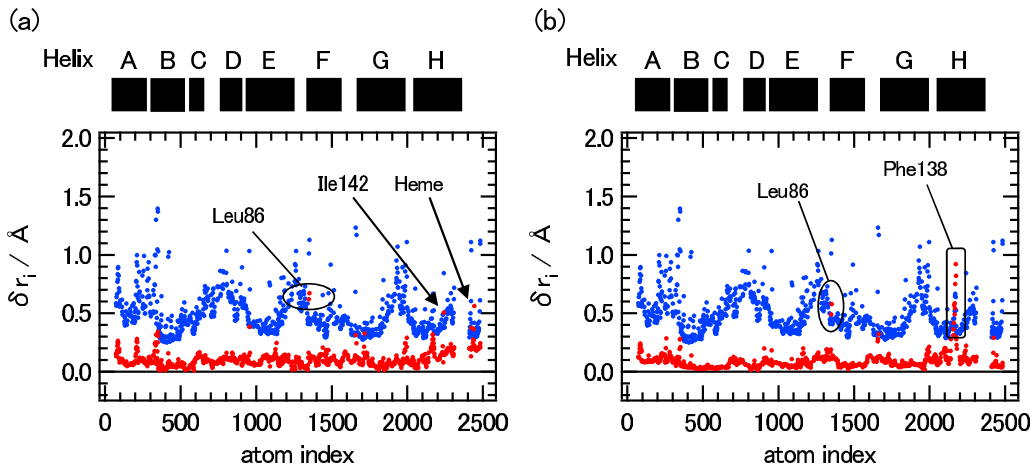


Figure S5: Protein conformational changes in response to the external forces coupled with the CO transitions between (a) Xe4 and Xe2, and (b) Xe2 and Xe1. Red dots represent protein responses and blue dots RMSF calculated from a 10-ns MD trajectory (the simulation (c) in Methods).

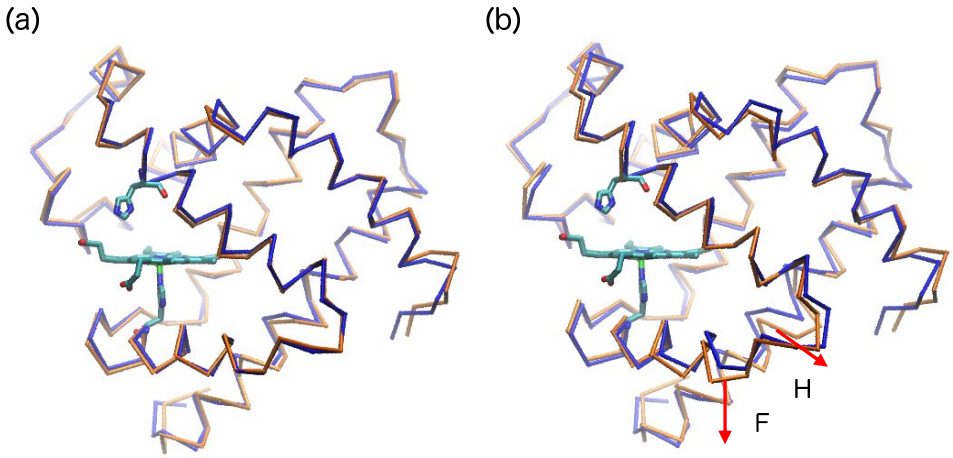


Figure S6: Protein backbone structural changes in response to the external forces coupled with the CO transitions between (a) Xe4 and Xe2, and (b) Xe2 and Xe1. Backbone traces of the average structure of the unperturbed deoxy Mb and of displaced structures undergoing the protein conformational changes in response to the external force are depicted in tube representation colored in blue and orange, respectively. Arrows in red along with labels of the helices indicate directions of the large conformational changes. To see the protein responses easily, the protein responses are depicted to be three times as large as one in Fig S5.

# 7 Contributions of the PC vectors to the protein responses coupled with the Xe4-to-Xe2 and Xe2-to-Xe1 transitions of CO

Figure S7 shows relative and accumulated relative contributions of the PC vectors to the protein displacements in response to the external forces coupled with Xe4-to-Xe2 and Xe2-to-Xe1 transitions of CO. The contributions to the protein response to the DP-to-Xe4 transition are described in Fig. 5.

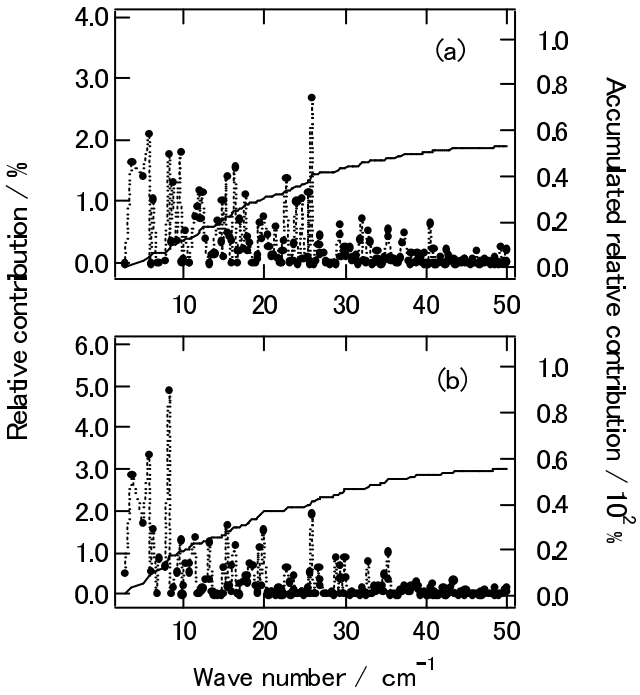


Figure S7: Relative contributions of PC vectors (dots and dotted lines) up to 50 cm$^{-1}$ and accumulated relative contributions (solid line) to protein conformational changes in response to the external forces coupled with the CO transitions between (a) Xe4 and Xe2, and (b) Xe2 and Xe1.

# 8 Derivation of a generalized Langevin equation given by Eq. (12)

A generalized Langevin equation given by Eq. (12) is derived by a procedure described in refs. (17, 18). A brief derivation is described below. As shown in Eq. (12), Hamiltonian that takes into account fluctuations up to the second order in an

$N$-dimensional PC space is expressed as,

$$H = \frac{1}{2}\dot{\boldsymbol{x}}^t\dot{\boldsymbol{x}} + \frac{1}{2}\boldsymbol{x}^t\boldsymbol{\omega}^2\boldsymbol{x} \tag{S5}$$

where $\boldsymbol{x}$ and $\boldsymbol{\omega}$ indicate coordinates of the protein in the PC space and their effective frequencies, respectively. Note that the frequency matrix $\boldsymbol{\omega}^2$ is diagonal in the PC space. The PC space is partitioned into two spaces, a one-dimensional space (vector) along the protein response, $\tilde{\mathbf{s}}$, given by Eq. (11) and the other $(N-1)$ space orthogonal to $\tilde{\mathbf{s}}$, $\tilde{\boldsymbol{U}}$. Those vector and matrix define the coordinates $S$ and $\boldsymbol{X}$ which represent the protein response and the coordinates orthogonal to $S$ by the relations of Eq. (10) and

$$\boldsymbol{X} = \tilde{\boldsymbol{U}}^t\boldsymbol{x} \tag{S6}$$

respectively. By the space partition, the potential term in Hamiltonian is rewritten with the coordinates $S$ and $\boldsymbol{X}$ as,

$$V = \frac{1}{2}\Omega^2 S^2 + \frac{1}{2}(\boldsymbol{X} + \tilde{\boldsymbol{\omega}}_{QQ}^{-2}\tilde{\boldsymbol{\omega}}_{QP}^2 S)^t\tilde{\boldsymbol{\omega}}_{QQ}^2(\boldsymbol{X} + \tilde{\boldsymbol{\omega}}_{QQ}^{-2}\tilde{\boldsymbol{\omega}}_{QP}^2 S) \tag{S7}$$

where

$$\Omega = \sqrt{\bar{\omega}^2 - \tilde{\boldsymbol{\omega}}_{PQ}^2\tilde{\boldsymbol{\omega}}_{QQ}^{-2}\tilde{\boldsymbol{\omega}}_{QP}^2}, \tag{S8}$$

$$\bar{\omega}^2 = \tilde{\mathbf{s}}^t\boldsymbol{\omega}^2\tilde{\mathbf{s}} = \sum_i \omega_i^2 s_i^2, \tag{S9}$$

$$\boldsymbol{\omega}_{QP}^2 = \boldsymbol{\omega}^2\tilde{\mathbf{s}} - \tilde{\mathbf{s}}\bar{\omega}^2 = \tilde{\boldsymbol{U}}\tilde{\boldsymbol{\omega}}_{QP}^2, \tag{S10}$$

$$\boldsymbol{\omega}_{PQ}^2 = \tilde{\mathbf{s}}^t\boldsymbol{\omega}^2 - \bar{\omega}^2\tilde{\mathbf{s}}^t = \tilde{\boldsymbol{\omega}}_{PQ}^2\tilde{\boldsymbol{U}}^t, \tag{S11}$$

$$\boldsymbol{\omega}_{QQ}^2 = \boldsymbol{\omega}^2 - \tilde{\mathbf{s}}\tilde{\mathbf{s}}^t\boldsymbol{\omega}^2 - \boldsymbol{\omega}^2\tilde{\mathbf{s}}\tilde{\mathbf{s}}^t + \tilde{\mathbf{s}}\bar{\omega}^2\tilde{\mathbf{s}}^t = \tilde{\boldsymbol{U}}\tilde{\boldsymbol{\omega}}_{QQ}^2\tilde{\boldsymbol{U}}^t. \tag{S12}$$

It is easily shown that an equation of motion for $S$ derived from Hamiltonian Eq. (S5) corresponds to a generalized Langevin equation for $S$ given by Eq. (12), i.e.,

$$\ddot{S} = -\Omega^2 S - \int_0^t \eta(t-t')\dot{S}(t')dt' + R(t) \tag{S13}$$

where $\eta(t)$ is the friction kernel expressed as

$$\eta(t) = \tilde{\boldsymbol{\omega}}_{PQ}^2\tilde{\boldsymbol{\omega}}_{QQ}^{-2}\cos(\tilde{\boldsymbol{\omega}}_{QQ}t)\tilde{\boldsymbol{\omega}}_{QP}^2, \tag{S14}$$

and satisfies the fluctuation-dissipation relation with the random force $R(t)$,

$$< R(0)R(t) >= k_{\mathrm{B}}T\eta(t). \tag{S15}$$

Time evolutions of the friction kernels are depicted in Fig. S8.

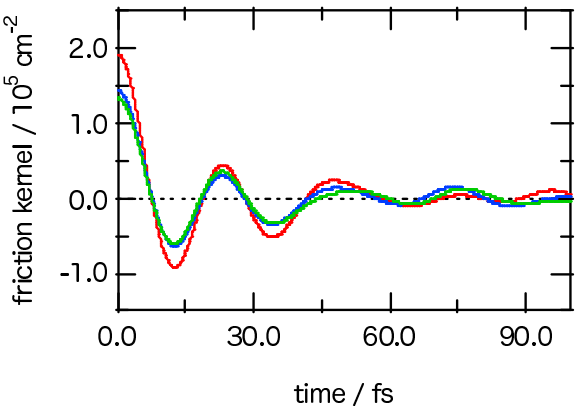


Figure S8: Time evolution of friction kernels $\eta(t)$. Red, blue and green lines represent $\eta(t)$ for the protein response motions coupled to the transitions between DP and Xe4, Xe4 and Xe2, and Xe2 and Xe1, respectively.

# 9 Expressions of MFPT

MFPT given by Eq. (1) was derived by Schulten et al. (19). Here, we briefly explain MFPT. For a double-well potential $V(x)$ along the reaction coordinate $x$, where two states, A and B, are separated by a potential barrier, the probability distribution is defined as

$$p_i(x) = Z_i^{-1} \exp(-V(x)/k_{\mathrm{B}}T) \begin{cases} x \le 0 & \text{if } i = \mathrm{A}\,, \\ x \ge 0 & \text{if } i = \mathrm{B} \end{cases}$$

where the barrier top is located at $x = 0$ and

$$Z_i = \int_{r_a}^{r_b} dx \exp(-V(x)/k_{\mathrm{B}}T) \begin{cases} r_a = -\infty \quad \text{and} \quad r_b = 0 & \text{if } i = \mathrm{A}\,, \\ r_a = 0 \quad \text{and} \quad r_b = \infty & \text{if } i = \mathrm{B}\,. \end{cases}$$

The probability distribution, $P_{\mathrm{CO}}(\boldsymbol{r})$, obtained in our previous study (4) was employed to calculate $p_i(x)$.

MFPT $\tau$ for the barrier crossing reaction A $\rightarrow$ B is

$$\tau = \tau_1 + \tau_{-2} Z_{\mathrm{A}}/Z_{\mathrm{B}} \tag{16}$$

where

$$\tau_i = \int_{r_a}^{r_b} dx [D(x)p_j(x)]^{-1} \left[ \int_{r_c}^{r_d} dy p_j(y) \right]^2$$

$$\begin{cases} j = \mathrm{A}, & r_a = -\infty, & r_b = 0, & r_c = -\infty, & \text{and} & r_d = x & \text{if } i{=}1, \\ j = \mathrm{B}, & r_a = 0, & r_b = \infty, & r_c = x, & \text{and} & r_d = \infty & \text{if } i{=}{-}2 \end{cases}$$

and $D(x)$ is the position dependent diffusion constant. We neglect the position dependences of the diffusion constants and employed diffusion constants evaluated at the barrier tops (see, the main text for discussions).

# 10 Evaluation of parameters in MFPT and TST rate expression

Parameters in MFPT and TST rate expressions $\omega_a$, $\gamma_a$ and $\gamma_b$, i.e., the frequency of the free energy well and the friction constants of the wells and the barrier tops were evaluated with the mean square displacements in the wells and around the barrier tops, respectively, obtained by MD simulations (the simulations (d-ii) and (e) described in Methods). A mean square displacement for an over-damped motion with a friction $\gamma$ in a harmonic well with a frequency $\omega$ is expressed as

$$\Delta R^2(t) = \Delta R^2(\infty)\left[1 - \exp\left(-\frac{\omega^2}{\gamma}t\right)\right]. \tag{S17}$$

The well frequency $\omega_a$ is therefore determined by

$$\omega_a = \sqrt{\frac{3k_{\mathrm{B}}T}{m\Delta R^2(\infty)}} \tag{S18}$$

where $m$ is the mass of CO. Relaxation time in the mean square displacement in an over-damped regime, $\tau = \gamma/\omega^2$, together with $\omega$ also determines the friction $\gamma$. Those quantities were evaluated by fitting them in Eq. (S17) to the mean square displacements computed by MD simulations as shown in Fig. S9.

The mean square displacements obtained by the MD simulations exhibit sharp rises in ~ 2 ps due to inertia motions followed by exponential increases representing the over-damped motions. Therefore, the latter relaxation curves (2 to 50 ps) were fitted to a modified functional form

$$\Delta R^2(t) = \Delta R^2(\infty) - A\exp(-t/\tau) \tag{S19}$$

where $\Delta R^2(\infty)$, $A$ and $\tau$ are the fitting parameters.

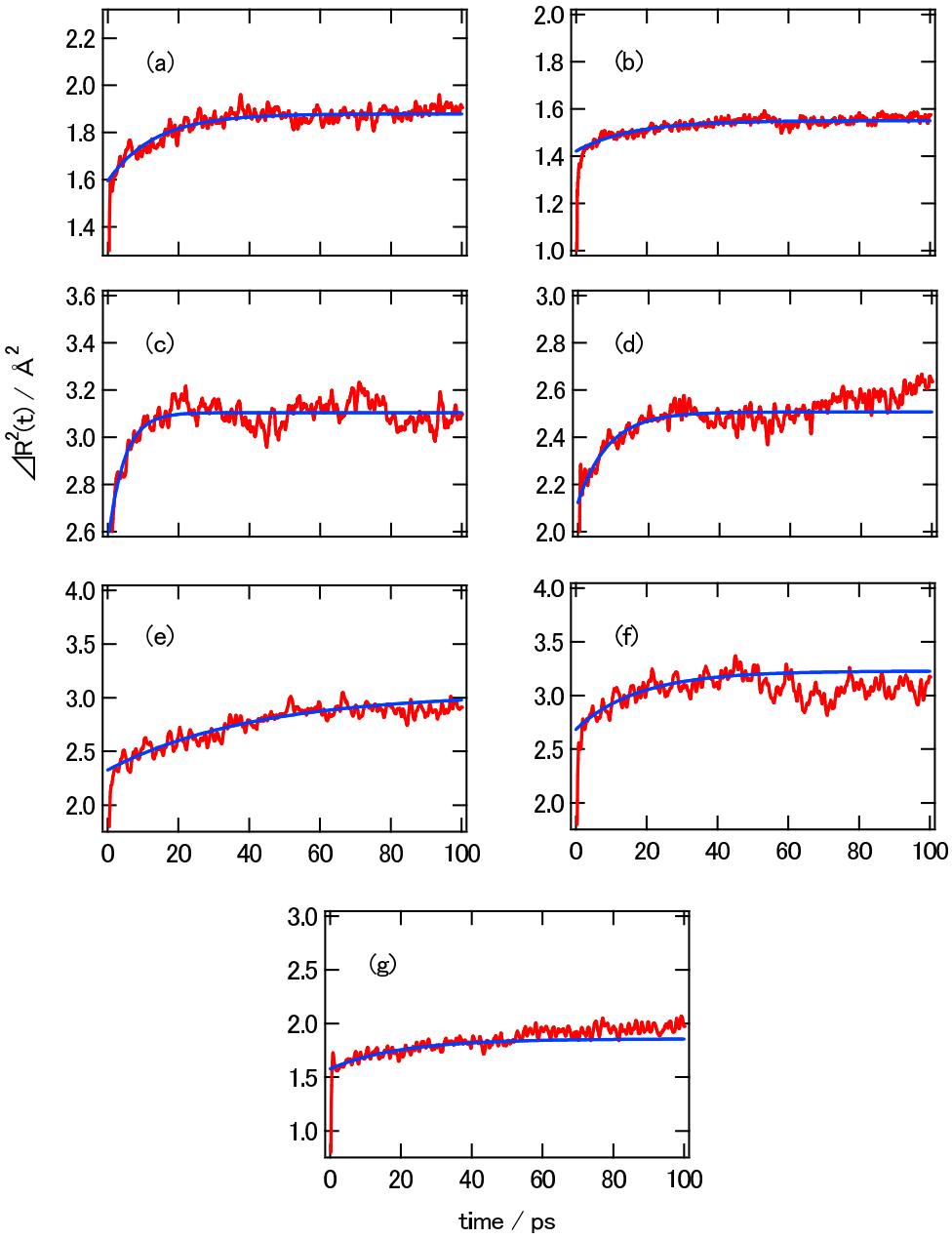


Figure S9: Mean square displacements in DP, Xe sites and barrier tops between neighboring sites obtained by MD simulations (red lines) and curves given by Eq. (S19) fitted to the MD displacements (blue lines). (a) DP, (b) Xe4, (c) Xe2, (d) Xe1, (e) between DP and Xe4, (f) between Xe4 and Xe2 and (g) between Xe2 and Xe1.

# References


[1] Wang, J., P. Cieplak, and P. Kollman, 2000. How well does a restrained electrostatic potential (RESP) model perform in calculating conformational energies of organic and biological molecules? *Journal of Computational Chemistry* 21:1049–1074.

[2] Jorgensen, W. L., J. Chandrasekhar, J. D. Madura, R. W. Impey, and M. L. Klein, 1983. Comparison of simple potential functions for simulating liquid water. *J. Chem. Phys.* 79:926–935.

[3] Giammona, D. A., 1984. An Examination of Conformational Flexibility in Porphyrins and Bulky-ligand Binding in Myoglobin. Ph.D. thesis, University of California, Davis.

[4] Nishihara, Y., S. Hayashi, and S. Kato, 2008. A search for ligand diffusion pathway in myoglobin using a metadynamics simulation. *Chem. Phys. Lett.* 464:220–225.

[5] Straub, J., and M. Karplus, 1991. Molecular dynamics study of the photodissociation of carbon monoxide from myoglobin: ligand dynamics in the first 10 ps. *Chem. Phys.* 158:221–248.

[6] Nutt, D., and M. Meuwly, 2003. Theoretical investigation of infrared spectra and pocket dynamics of photodissociated carbonmonoxy myolgobin. *Biophs, J.* 85:3612–3623.

[7] Nutt, D., and M. Meuwly, 2004. CO migration in native and mutant myoglobin: Atomistic simulations for the understanding of protein function. *Proc. Natl. Acad. Sci. U.S.A.* 101:5998–6002.

[8] Plattner, N., and M. Meuwly, 2008. The Role of Higher CO-Multipole Moments in Understanding the Dynamics of Photodissociated Carbonmonoxide in Myoglobin. *Biophys.J.* 94:2505–2515.

[9] Banushkina, P., and M. Meuwly, 2007. Diffusive dynamics on multidimensional rough free energy surfaces. *J. Chem. Phys.* 127:135101.

[10] Hummer, G., F. Schotte, and P. A. Anfinrud, 2004. Unveiling functional protein motions with picosecond x-ray crystallography and molecular dynamics simulations. *Proc. Natl. Acad. Sci. U.S.A.* 101:15330–15334.

[11] Berendsen, H. J. C., J. P. M. Postma, W. F. van Gunsteren, A. DiNola, and J. R. Haak, 1984. Molecular dynamics with coupling to an external bath. *J. Chem. Phys.* 81:3684–3690.

[12] Darden, T., D. York, and L. Pedersen, 1993. Particle mesh Ewald: an $N\cdot\log(N)$ method for Ewald sums in large systems. *J. Chem. Phys.* 98:10089–10092.

[13] Ryckaert, J. P., G. Ciccotti, and H. J. C. Berendsen, 1977. Numerical integration of the cartesian equations of motion of a system with constraints: molecular dynamics of *n*-alkanes. *J. Computat. Phys.* 23:327–341.

[14] Šrajer, V., Z. Ren, T. Y. Teng, M. Schmidt, T. Ursby, D. Bourgeois, C. Pradervand, W. Schildkamp, M. Wulff, and K. Moffat, 2001. Protein conformational relaxation and ligand migration in myoglobin: a nanosecond to millisecond molecular movie from time-resolved Laue X-ray diffraction. *Biochemistry* 40:13802–13815.

[15] Schotte, F., J. Soman, J. S. Olson, M. Wulff, and P. A. Anfinrud, 2004. Picosecond time-resolved X-ray crystallography: probing protein function in real time. *J. Struct. Biol.* 147:235–246.

[16] Cohen, J., A. Arkhipov, R. Braun, and K. Schulten, 2006. Imaging the migration pathways for $O_2$, CO, NO, and Xe inside myoglobin. *Biophys. J.* 91:1844–1857.

[17] Ando, K., and S. Kato, 1991. Dielectric relaxation dynamics of water and methanol solutions associated with the ionization of *N*, *N*-dimethylaniline: theoretical analyses. *J. Chem. Phys.* 95:5966–5982.

[18] Hayashi, S., K. Ando, and S. Kato, 1995. Reaction dynamics of charge-transfer state formation of 4-(*N*, *N*-dimethylamino) benzonitrile in a methanol solution: theoretical analyses. *J. Phys. Chem.* 99:955–964.

[19] Schulten, K., Z. Schulten, and A. Szabo, 1981. Dynamics of reactions involving diffusive barrier crossing. *J. Chem. Phys.* 74:4426–4432.